

Charge state readout and hyperfine interaction in a few-electron InGaAs double quantum dotM. Larsson¹ and H. Q. Xu^{1,2,*}¹*Division of Solid State Physics, Lund University, P.O. Box 118, SE-221 00 Lund, Sweden*²*Department of Electronics and Key Laboratory for the Physics and Chemistry of Nanodevices, Peking University, Beijing 100871, China*

(Received 21 January 2011; revised manuscript received 5 April 2011; published 1 June 2011)

A laterally defined InGaAs double quantum dot with an integrated charge readout sensor is realized in an InGaAs/InP heterostructure. The charge states of the double quantum dot are measured with the use of the charge readout sensor in the few-electron regime in which the current is too weak to be observable by direct measurements of electron transport through the double dot. We also measure the leakage current of the double quantum dot in the Pauli spin-blockade few-electron regime and study the singlet-triplet state mixing by the hyperfine coupling to the nuclear spins. The measurements of the leakage current in the weak external-magnetic-field region and for weak interdot couplings allow us to extract an effective nuclear magnetic field in the double-dot system. We also study spin relaxation and transport processes in the Pauli spin-blockade region at large external magnetic fields and observe transport through the excited triplet state in the few-electron double quantum dot.

DOI: [10.1103/PhysRevB.83.235302](https://doi.org/10.1103/PhysRevB.83.235302)

PACS number(s): 73.23.Hk, 73.63.Kv, 72.25.Rb

I. INTRODUCTION

The control of electron spins in few-electron quantum dots has seen intensive interest and progress in the last couple of years since a proposal to use double quantum dots as spin qubits for quantum-information processing^{1,2} first appeared. The hyperfine coupling between the electron spins on the dots and the surrounding nuclei has a fundamental effect on spin transport and is a source of spin decoherence in materials with a nonzero nuclear spin.^{3–7} In order to control the spin decoherence in these systems, knowledge of state-mixing induced by the electron-nuclear interaction is critical.^{8,9} Additionally, the hyperfine coupling to the nuclear spins could be used to store quantum information.^{10,11} Double quantum dots were first realized primarily in high-electron-mobility GaAs/AlGaAs heterostructures.^{12,13} These laterally defined double quantum dots can be integrated with a charge readout sensor and have been extensively used in charge-detection experiments,^{14–17} coupled-spin-manipulation experiments,¹⁸ and measurements of spin relaxation due to the hyperfine coupling to nuclear spins.^{3,4} However, due to a negligibly small Rashba spin-orbit coupling coefficient in GaAs/AlGaAs heterostructures,¹⁹ it is difficult to control the spins in the quantum dots and the coupling between spins in the neighboring quantum dots by an electrical way desired for quantum information processing applications. Vertically configured double quantum dots have been realized with InAs-based heterostructures.^{8,20} Double quantum dots have also been realized with InAs nanowires.^{6,21,22} The large spin-orbit-coupling coefficients in these material systems make InAs-based double quantum dots one of the most promising platforms for solid-state-based quantum-information processing. However, in both the vertically configured double quantum dots and the nanowire double quantum dots, it is technically very challenging to integrate a high-performance charge readout element, although such an integration is not absolutely impossible.^{23–25}

Here, we report the realization and measurements of a laterally defined few-electron double quantum dot in an InGaAs/InP heterostructure with an integrated quantum point contact (QPC) charge-readout sensor. Recently, progress has been made in the fabrication of lateral single- and double-

quantum-dot devices in InGaAs/InP heterostructures.^{26–29} The large g factor^{26,27} and tunable spin-orbit interaction³⁰ in the materials make InGaAs-quantum-dot systems yet another promising platform for quantum-information-processing applications. However, it is very difficult to achieve a high-performance few-electron-quantum-dot device with an integrated charge readout sensor in an In-contained heterostructure by top-gate technology. In this work, a technology of combining etched trenches and fine finger gates is developed for defining high-performance quantum devices in In-contained heterostructures and is employed for the fabrication of our double-dot device in an InGaAs/InP heterostructure. With the help of the charge-readout sensor, we tune our fabricated double-dot device to the last few-electron charge-state configurations and study the singlet-triplet state mixing caused by the hyperfine coupling in the Pauli-spin-blockade region. In particular, the magnetic-field dependence of the leakage current is analyzed for different interdot tunnel couplings and at different levels of detuning. Based on the analysis, an effective nuclear magnetic field of the order of a few millitesla in strength in the double-quantum-dot system is extracted. We also study spin relaxation and transport processes in the Pauli-spin-blockade condition at large external magnetic fields and observe transport through the excited triplet state in the double quantum dot.

II. EXPERIMENTAL TECHNIQUES

The device studied in this work is fabricated in a modulation-doped $\text{In}_{0.75}\text{Ga}_{0.25}\text{As}/\text{InP}$ heterostructure containing a two-dimensional electron gas (2DEG) in a 9-nm-thick InGaAs quantum-well layer located 40 nm below the surface. At a temperature of 300 mK, the 2DEG shows a mobility and a sheet electron concentration of $1.0 \times 10^5 \text{ cm}^2\text{V}^{-1}\text{s}^{-1}$ and $7.5 \times 10^{11} \text{ cm}^{-2}$, respectively. By electron beam lithography (EBL) and wet chemical etching, a 700-nm-long and 150-nm-wide quantum wire is defined in the 2DEG. A QPC with a width of 250 nm is simultaneously defined in close proximity to the quantum wire. By atomic-layer deposition, a 20-nm-thick HfO_2 film is grown locally on the top of the

device, acting as a gate dielectric. Finally, six local finger Ti-Au gates are deposited over the device by EBL and thermal evaporation. Among them, five finger gates are placed locally over the quantum wire and the remaining one is on the top of the QPC. The width of the finger gates is about 40 nm and the periodicity of those five finger gates over the quantum wire is 80 nm. Figure 1(a) shows a scanning-electron-microscope image of the fabricated device.

Transport measurements are performed in a dilution refrigerator at a base temperature of about 100 mK. A dc bias voltage, V_{sd} , is applied symmetrically between the source and drain contacts of the double quantum dot and a dc bias voltage, $V_{sd,QPC}$, is applied between the QPC contacts. Negative dc voltages are applied to the local finger gates, lg1, lg3, and lg5, to induce electrostatic tunnel barriers along the quantum wire to form a double quantum dot. Here, gates lg1 and lg5 are used to set the coupling to the source and drain reservoirs and gate lg3 is used to tune the interdot coupling. Gates lg2 and lg4 are used to tune the energy levels of the left and right dots while the QPC conductance is tuned by gate lgq to allow sensing of the charge states in the double quantum dot.³¹ To achieve a maximum sensitivity, the conductance of the QPC is tuned to the region of $G_{QPC} < 2e^2/h$, where the transconductance dI_{QPC}/dV_{lgq} is high.

voltage, V_{sd} , is applied symmetrically between the source and drain contacts of the double quantum dot and a dc bias voltage, $V_{sd,QPC}$, is applied between the QPC contacts. Negative dc voltages are applied to the local finger gates, lg1, lg3, and lg5, to induce electrostatic tunnel barriers along the quantum wire to form a double quantum dot. Here, gates lg1 and lg5 are used to set the coupling to the source and drain reservoirs and gate lg3 is used to tune the interdot coupling. Gates lg2 and lg4 are used to tune the energy levels of the left and right dots while the QPC conductance is tuned by gate lgq to allow sensing of the charge states in the double quantum dot.³¹ To achieve a maximum sensitivity, the conductance of the QPC is tuned to the region of $G_{QPC} < 2e^2/h$, where the transconductance dI_{QPC}/dV_{lgq} is high.

III. TRANSPORT AND CHARGE STATE READOUT MEASUREMENTS

Figure 1(b) shows the conductance through the double quantum dot, created by setting $V_{lg1} = -380$ mV, $V_{lg3} = -180$ mV, and $V_{lg5} = -420$ mV, as a function of V_{lg2} and V_{lg4} in the linear-response regime on a logarithmic color scale. Hexagon patterns of high conductance, typical for the electron transport through a double quantum dot, can be clearly seen in the figure. The finite conductance lines caused by cotunneling, connecting the degeneracy points, i.e., the hexagon corners, indicate that the system is in the strong interdot-coupling region. Figure 1(c) shows the transconductance, dI_{QPC}/dV_{lg2} , of the charge readout QPC as a function of V_{lg2} and V_{lg4} measured simultaneously with the data presented in Fig. 1(b) with $V_{sd,QPC} = 1$ mV. Dips in the transconductance, corresponding to the changes in the charge states of the two dots, are clearly seen as white lines, which overlap nicely with the conductance peaks in Fig. 1(b). With this gate voltage configuration, the number of electrons in each dot is around 10. By monitoring the QPC conductance, the charge state (m, n) , where m and n are the numbers of electrons on the left and right quantum dots, can be determined even in the case when the current through the double quantum dot is too small to be measured in our experimental setup. Figure 1(d) shows the conductance of the QPC in the gate-voltage region where each quantum dot contains two or less electrons. Here, as in Ref. 15, a background-conductance plane is subtracted in order to more clearly see the charge-state dependence of the QPC conductance. The static gate voltages used in this measurement are $V_{lg1} = -370$ mV, $V_{lg3} = -200$ mV, and $V_{lg5} = -420$ mV. Figure 1(e) shows a close-up view of the region marked by the dashed lines in Fig. 1(d). Four constant values of the conductance, corresponding to the four different charge-state configurations, i.e., $(0, 0)$, $(0, 1)$, $(1, 0)$ and $(1, 1)$, are clearly seen in the figure. Figure 1(f) shows traces of the real QPC conductance along the dashed lines in Fig. 1(e). The jump in the conductance, corresponding to a unit change in the number of electrons on the left dot, is about $\Delta G_{left} = 0.3 \times 10^{-3} e^2/h$, and it is about $\Delta G_{right} = 0.1 \times 10^{-3} e^2/h$ for a unit change in the number of electrons on the right dot. However, the current through the double quantum dot at these charge states is completely suppressed or it is too small to be measured due to the weak tunnel couplings of the double dot to the source and drain leads.

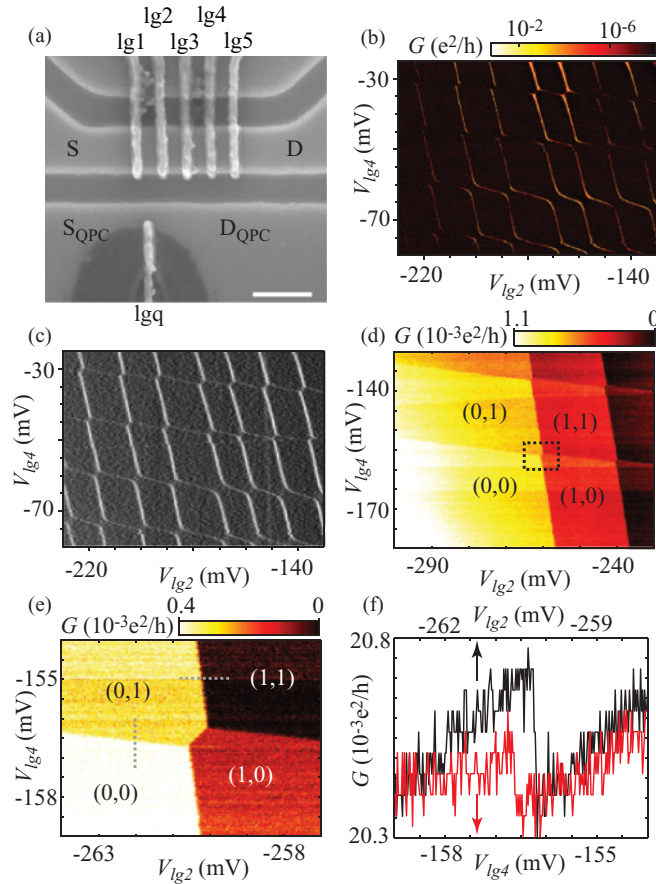


FIG. 1. (Color online) (a) Scanning-electron-microscope image of the measured device. The five gates over the quantum wire define a double quantum dot while the QPC is used as a charge readout to probe the charge states of the double quantum dot. The scale bar is 200 nm. (b) Charge-stability diagram showing the conductance through the double quantum dot as a function of V_{lg2} and V_{lg4} in the regime of strong interdot coupling on a logarithmic color scale. (c) Charge-stability diagram showing the transconductance, dI_{QPC}/dV_{lg2} , of the charge readout QPC as a function of V_{lg2} and V_{lg4} measured simultaneously with (b). (d) Conductance of the charge readout QPC as a function of V_{lg2} and V_{lg4} (charge-stability diagram) in the few-electron regime. Here, a background-conductance plane is subtracted. The levels of the conductance seen in the figure correspond to different charge-state configurations. Four charge states are indicated by labels (m, n) in this figure, where m and n are the exact numbers of electrons in the left and right dots, respectively. (e) Close-up view of the region marked by the dashed lines in (d). (f) Traces along the dashed lines in (e) showing the actually measured QPC conductance as a function of gate voltage.

IV. PAULI SPIN BLOCKADE AND TRIPLET TO SINGLET RELAXATION VIA HYPERFINE INTERACTION

Figure 2(a) shows a stability diagram of the current through the double quantum dot in the $(2,6) \rightarrow (3,5)$ charge-state transition at a finite bias voltage of $V_{sd} = 1$ mV, where the current through the device is large enough to be measured. The static gate voltages used in this and the following measurements are $V_{lg1} = -390$ mV and $V_{lg5} = -440$ mV with the voltage of V_{lg3} indicated in the figures. At a finite bias voltage, the degeneracy points, or triple points, have developed into triangular regions [outlined by the white dashed lines in Fig. 2(a)] of finite current, where the size of the triangles is determined by the applied bias voltage.¹³ Along the base line of the triangles, the chemical potentials of the two dots are aligned and within the bias voltage window and the resonant transport through the double-quantum-dot system via singlet states can occur. Inside the triangular area, the chemical potentials of the two dots are detuned and the transport is inelastic, resulting in a smaller current than for the resonant case. Outside of the triangular regions, electron transport is Coulomb blocked. Figure 2(b) shows the current through the double quantum dot via the $(3,5) \rightarrow (2,6)$ charge state transition at a negative bias voltage of $V_{sd} = -1$ mV with $V_{lg3} = -255$ mV. The triangles are now mirrored with respect to the triangle baseline and we see that the current is strongly suppressed at the baseline, except at the baseline edges. We also see a new line of high current running parallel to the baseline at a constant detuning, Δ , of the energy levels in the two dots. This current-rectification behavior can be explained by Pauli spin blockade.^{20,32}

In the following discussion, it is enough to only consider the spin states of unpaired spins in the dots. We will therefore refer to the $(2,5)$ charge state as the $[0,1]$ state, since the two excess spins of the electrons in the left dot and the four excess spins of the electrons in the right dot pair off. Similarly, the $(3,5)$ charge state will be referred to as the $[1,1]$ state and the $(2,6)$ charge state as the $[0,2]$ state. We now investigate the $[1,1] \rightarrow [0,2]$ transition in more detail. In the $[1,1]$ state configuration, one excess electron is assumed to occupy the right dot, while the left dot is loaded by an electron from the left lead. In the limit of weak interdot tunnel coupling, the exchange energy is small and the two electrons in the different dots can be considered almost independent. Therefore, the electron entering the left dot can be loaded either into the singlet $[1,1]_s$ state or into a triplet $[1,1]_t$ state of the double quantum dot. If a spin-down electron enters the left dot, the double-dot system is in the $[1,1]_s$ state, see the left diagram in Fig. 2(d). This electron can tunnel to the right dot to form a $[0,2]_s$ singlet state and, finally, leave the double-quantum-dot system through the right lead. However, if a spin-up electron is loaded into the left dot to form a double-dot triplet $[1,1]_t$ state, this spin-up electron can not tunnel to the right dot since the $[0,2]_t$ triplet states are too high in energy, nor can it tunnel back to the left lead if the state is below the Fermi level, see the right diagram in Fig. 2(d). Transport is therefore blocked, this is referred to as Pauli spin blockade. At the lower edge of the triangle baseline, there is a small increase in current. Here, a spin-up electron loaded into the $[1,1]_t$ state is within the thermally broadened Fermi level of the left lead. The electron

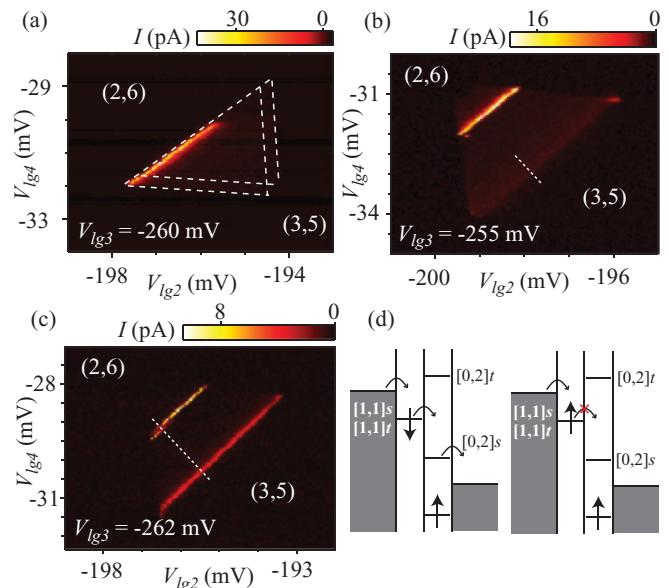


FIG. 2. (Color online) (a) Current through the double quantum dot at the $(2,6) \rightarrow (3,5)$ charge-state transition showing a pair of triple-point triangular regions of high current at a finite positive bias voltage of $V_{sd} = 1$ mV. (b) and (c) Current through the double quantum dot at a negative-bias voltage of $V_{sd} = -1$ mV with $V_{lg3} = -255$ mV and $V_{lg3} = -262$ mV, respectively. Pauli spin blockade results in a suppression of the current in the triangle region. The line of high current, which is parallel to the triangle base line, corresponds to the electron transport through an excited triplet state at a large finite detuning. (d) Schematic energy diagram showing sequential tunneling through the double quantum dot when the left dot is loaded with a spin-down electron (left) and Pauli spin blockade when the left dot is loaded with a spin-up electron (right).

can therefore tunnel out to the left lead and be replaced by a spin-down electron. This spin-down electron can then tunnel to the right lead through the $[0,2]_s$ state. At the upper edge of the triangle baseline, there is an equivalent hole cycle leading to an increase in the current. The high-current line that runs parallel with the triangle baseline marks the point where the $[0,2]_t$ states are aligned with the chemical potential of the left dot and resonant transport through the double quantum dot via the $[0,2]_t$ states becomes possible. In Fig. 2(c), the tunnel coupling between the two dots has been reduced by setting $V_{lg3} = -262$ mV. This reduction has resulted in an increase in the leakage current along the triangle baseline, indicating that the triplet to singlet relaxation in the double dot is enhanced.

The triplet to singlet relaxation leading to an increase in leakage current in the Pauli-spin-blockade region seen in Fig. 2(c) can be attributed to the hyperfine coupling of the electron spin with the nuclear spins as has previously been reported for GaAs and InAs double-quantum-dot systems.^{3,4,6} The random unpolarized and uncorrelated nuclear spins in the two dots yield an inhomogeneous effective nuclear magnetic field (so-called Overhauser field) pointing in a random direction with a strength, B_n , of the order of a few mT for the dot sizes studied here.^{3,6} This effective nuclear magnetic field gives rise to a mixing of the $[1,1]_s$ and $[1,1]_t$ states when $E_n > E_{st}$, where $E_n = |g^*| \mu_B B_n$ is the Zeeman splitting energy of the two spin states caused by the effective nuclear

magnetic field and $E_{st} = |E_{[1,1]s} - E_{[1,1]t}|$ is the singlet-triplet splitting energy.

Figure 3(a) shows the current through the double quantum dot as a function of external magnetic field, B , applied parallel to the quantum wire and level detuning, Δ , measured along the white dashed line in Fig. 2(c). Here, the gate voltage has been converted to energy. The high current peak around zero field and zero detuning is the leakage current caused by sequential transport through the $[1,1]s$ and $[0,2]s$ states. The peak is clearly suppressed and moves toward higher detuning at larger fields. This is caused by the split-off $[1,1]t_+$ state at the applied magnetic field. Transport through this level is unlikely since it requires a spin flip to occur and therefore the current is suppressed. However, when the $[1,1]t_+$ state is aligned with the $[0,2]s$ state, nuclear-field mixing is possible and results in a weak current peak. The current peak at $\Delta = 0.7$ meV is caused by sequential tunneling through the $[1,1]t$ and $[0,2]t$ states and does not change with the applied magnetic field. The two weak peaks splitting off from the strong triplet peak correspond to the $[1,1]t_+ \rightarrow [0,2]t_0$ and $[1,1]t_0 \rightarrow [0,2]t_+$ transport processes (positive slope) and to the $[1,1]t_0 \rightarrow [0,2]t_+$ and $[1,1]t_- \rightarrow [0,2]t_0$ transport processes (negative slope), respectively. Transport through these levels require higher-order spin-flip processes and thus results in a current peak weaker than the $\Delta = 0.7$ -meV peak. By fitting the magnetic-field dependencies of the two weak peaks, a g factor of 2.3 was extracted for an electron in the double-dot system. This value is in a good agreement with the previous studies of few-electron quantum dots made in the same material system.²⁷

Figure 3(b) shows a close-up view of the area within the white dashed lines in Fig. 3(a). The influence of the effective-nuclear-field mixing of the singlet and triplet states on the leakage current in the Pauli spin-blockade region is more clearly seen in this figure. For a small interdot coupling, the leakage current is at a maximum at zero detuning and zero magnetic field [see Fig. 3(b)]. However, in the case of a larger interdot coupling [see Fig. 3(c)], the leakage current has a minimum at zero detuning and zero magnetic field and is enhanced with the increase of detuning or the increase of external magnetic field. This behavior of the leakage current can be explained by considering the different competing energy scales given by: the Zeeman-splitting energy, $E_{ext} = |g^*|\mu_B B$, caused by the external magnetic field, the Zeeman-splitting energy from the effective nuclear field, $E_n = |g^*|\mu_B B_n$, and the splitting energy, E_{st} , between the triplet states $[1,1]t$ and the singlet states, i.e., hybrid states of the $[1,1]s$ and $[0,2]s$ states. This singlet-triplet splitting is effectively controlled by the interdot tunnel coupling set by V_{lg3} and the detuning. At $\Delta = 0$, the hybridization of the $[1,1]s$ and $[0,2]s$ states gives rise to an anticrossing [see Fig. 3(d)], where the energy gap (indicated by two short blue solid arrows) depends on the interdot coupling. A smaller interdot coupling gives rise to a smaller energy gap [blue solid lines in Fig. 3(d)], while a larger coupling gives rise to a large energy gap [gray dashed lines in Fig. 3(d)]. Efficient mixing of the singlet and triplet $[1,1]$ states is only possible when the splitting from the nuclear field, E_n , of the $[1,1]t$ state is larger than the singlet-triplet splitting, E_{st} . For a small interdot coupling this leads to efficient mixing at small detuning [as well as over the

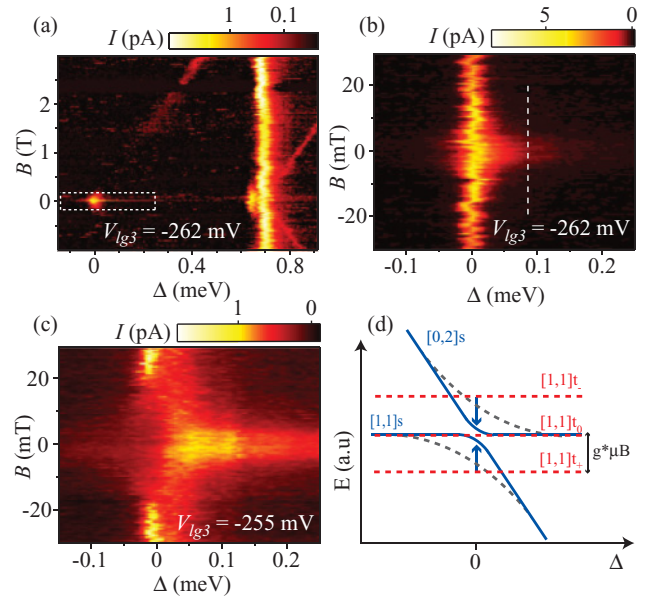


FIG. 3. (Color online) (a) Current through the double quantum dot as a function of external applied magnetic field and detuning cut along the dashed white line in Fig. 2(c). (b) Zoom-in view of the area within the white dashed line in Fig. 3(a). (c) The same measurement as in (b) but with a smaller interdot tunnel coupling. (d) Schematic representation of the energy evolution of the $[1,1]s$, $[1,1]t$, and $[0,2]s$ states as a function of detuning, Δ . The hybridization of the $[1,1]s$ and $[0,2]s$ due to the finite interdot coupling leads to an anticrossing at $\Delta = 0$. The blue solid lines correspond to a small interdot coupling while the blue dashed lines correspond to a larger interdot coupling. At a finite external magnetic field, the triplet state splits into three levels (dashed red lines).

whole range of detuning in Fig. 3(b)], while for a large interdot coupling, the mixing is possible only at finite detunings [see Fig. 3(c)]. At a finite external magnetic field, the $[1,1]t$ triplet state will split. This can result in a decrease in leakage current in the weak-interdot-tunnel-coupling case [Fig. 3(b)]. However, in a strong-interdot-coupling case, the split triplet states $[1,1]t_{\pm}$ may move closer to the two well-separated hybrid-singlet states at the zero and small detunings, and can therefore enhance the mixing of the triplet states with the singlet states via the random nuclear magnetic field. In this finite-magnetic-field situation, the triplet states may also decay to the singlet $[0,2]s$ states via spin-orbit interaction. Physically, both processes will result in an increase in leakage current at a finite magnetic field the strong-interdot-coupling case, as seen in Fig. 3(c). Nevertheless, at sufficiently large detunings, an application of an external magnetic field will suppress the leakage current in both weak- and strong-interdot-tunnel-coupling cases considered in Figs. 3(b) and 3(c).

The magnetic-field dependence of the leakage current at large detuning and weak interdot coupling can be used to extract the value of the strength of nuclear magnetic fields in the system. Figure 4(a) shows the leakage current measured at detuning $\Delta = 80 \mu\text{eV}$ against the applied magnetic field [i.e., along the white dashed line in Fig. 3(b)] at three different weak interdot couplings. Theoretical fits of the experimental data, based on the quantitative description presented in Ref. 5,

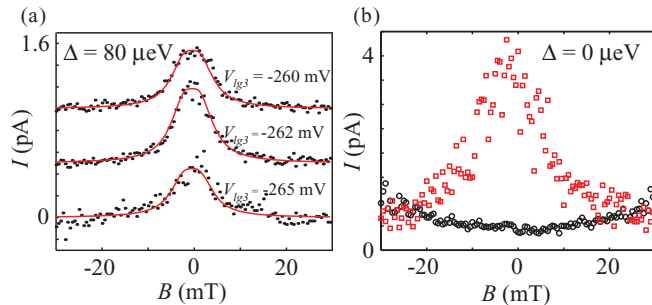


FIG. 4. (Color online) (a) Plots of the leakage current as a function of the applied external magnetic field at detuning $\Delta = 80 \mu\text{eV}$ [i.e., along the white dashed line in Fig. 3(b)] at three different weak interdot couplings. Solid lines are theoretical fits of the experimental data. Offsets have been added to the two upper plots for clarity. (b) Plots of the leakage current as a function of the applied external magnetic field at detuning $\Delta = 0 \mu\text{eV}$ in a weak-interdot-coupling case of $V_{lg3} = -265 \text{ mV}$ (squares) and a strong-interdot-coupling case of $V_{lg3} = -255 \text{ mV}$ (circles).

are included as solid lines in the figure. The formula adopted from Ref. 5 for the average current is

$$\langle I \rangle / e = \Gamma_{\text{in}} S(\sqrt{3}B/B_n),$$

where Γ_{in} is the tunneling rate and

$$S(x) = 4/x^2 - 6/x^4 + \sqrt{2\pi} \text{erfi}(x/\sqrt{2})(6/x^5 - 2/x^3) \times \exp(-x^2/2) - 3\pi \text{erfi}^2(x/\sqrt{2}) \exp(-x^2)/x^6.$$

In the fits to the measured data presented in Fig. 4(a), a nuclear-field strength $B_n = 2.7 \text{ mT}$ is extracted. This magnetic-field strength is similar to the previously reported values for GaAs (see Ref. 3) and InAs (see Ref. 6) double-quantum-dot systems. Using the experimentally extracted values of g^* and B_n we calculate $E_n = 0.4 \mu\text{eV}$.

Finally, we note that recent theoretical and experimental investigations of the competition between hyperfine and spin-orbit mixing of the singlet and triplet states in a spin-blockaded double quantum dot have shown that the interdot coupling plays a fundamental role in determining the spin-relaxation mechanism.^{21,22,33} In the weak-interdot-coupling regime, the hyperfine mixing is expected to dominate in lifting the spin

blockade. In this regime, a peak in the leakage current centered around zero magnetic field and zero detuning is expected. In the strong-coupling regime and a large magnetic field, spin-orbit mixing is expected to play a major role in lifting spin blockade, giving a dip around zero magnetic field and zero detuning.^{21,22,33} Figure 3(b) is in qualitative agreement with the hyperfine-dominated mixing case showing a peak in the leakage current for $\Delta = 0 \text{ meV}$ around zero magnetic field. In the case of strong coupling seen in Fig. 3(c), the peak has transitioned into a weak dip around zero magnetic field, which could be an indication that the system is in the regime where the hyperfine- and spin-orbit-interaction contributions to the leakage current are comparable in size. Figure 4(b) shows the measured leakage current as a function of magnetic field at zero detuning for a weak- and a strong-interdot-coupling case. Here, the peak and dip in the leakage current around zero field are clearly seen. However, in this study, we did not reach the extremely strong interdot coupling regime in which the current will show a well-defined dip at zero magnetic field.^{21,22,33}

V. CONCLUSIONS

In conclusion, we have reported on a charge-sensing experiment and leakage-current measurements in the Pauli-spin-blockade regime of a few-electron double quantum dot. The device is defined in an $\text{In}_{0.75}\text{Ga}_{0.25}\text{As}$ quantum well by etched trenches and top-finger gates. The magnetic-field dependence of the leakage current has been analyzed in detail for different interdot tunnel couplings and at different levels of detuning. Based on the analysis, an effective nuclear magnetic field of strength $\sim 2.7 \text{ mT}$ has been extracted for the double-quantum-dot system. Further investigation of the leakage current in the strong-interdot-coupling regime is necessary to determine the effect of spin-orbit interaction on the electron spin dynamics of the double-quantum-dot system.^{21,22,33}

ACKNOWLEDGMENTS

This work, which was performed at the Nanometer Structure Consortium at Lund University (nmC@LU), has been supported by the Swedish Research Council (VR).

*hongqi.xu@ftf.lth.se

¹D. Loss and D. P. DiVincenzo, *Phys. Rev. A* **57**, 120 (1998).

²R. Hanson, L. P. Kouwenhoven, J. R. Petta, S. Tarucha, and L. M. K. Vandersypen, *Rev. Mod. Phys.* **79**, 1217 (2007).

³F. H. L. Koppens, J. A. Folk, J. M. Elzerman, R. Hanson, L. H. Willems van Beveren, I. T. Vink, H. P. Tranitz, W. Wegscheider, L. P. Kouwenhoven, and L. M. K. Vandersypen, *Science* **309**, 1346 (2005).

⁴A. C. Johnson, J. R. Petta, J. M. Taylor, A. Yacoby, M. D. Lukin, C. M. Marcus, M. P. Hanson, and A. C. Gossard, *Nature (London)* **435**, 925 (2005).

⁵O. N. Jouravlev and Y. V. Nazarov, *Phys. Rev. Lett.* **96**, 176804 (2006).

⁶A. Pfund, I. Shorubalko, K. Ensslin, and R. Leturcq, *Phys. Rev. B* **76**, 161308(R) (2007).

⁷H. O. H. Churchill, A. J. Bestwick, J. W. Harlow, F. Kuemmeth, D. Marcos, C. H. Stwertka, S. K. Watson, and C. M. Marcus, *Nat. Phys.* **5**, 321 (2009).

⁸K. Ono and S. Tarucha, *Phys. Rev. Lett.* **92**, 256803 (2004).

⁹D. J. Reilly, J. M. Taylor, J. R. Petta, C. M. Marcus, M. P. Hanson, and A. C. Gossard, *Science* **321**, 817 (2008).

¹⁰B. E. Kane, *Nature (London)* **393**, 133 (1998).

¹¹J. M. Taylor, C. M. Marcus, and M. D. Lukin, *Phys. Rev. Lett.* **90**, 206803 (2003).

¹²N. C. van der Vaart, S. F. Godijn, Y. V. Nazarov, C. J. P. M. Harmans, J. E. Mooij, L. W. Molenkamp, and C. T. Foxon, *Phys. Rev. Lett.* **74**, 4702 (1995).

- ¹³W. G. van der Wiel, S. De Franceschi, J. M. Elzerman, T. Fujisawa, S. Tarucha, and L. P. Kouwenhoven, *Rev. Mod. Phys.* **75**, 1 (2003).
- ¹⁴J. M. Elzerman, R. Hanson, J. S. Greidanus, L. H. Willems van Beveren, S. De Franceschi, L. M. K. Vandersypen, S. Tarucha, and L. P. Kouwenhoven, *Phys. Rev. B* **67**, 161308 (2003).
- ¹⁵T. Fujisawa, T. Hayashi, R. Tomita, and Y. Hirayama, *Science* **312**, 1634 (2006).
- ¹⁶S. Gustavsson, R. Leturcq, M. Studer, T. Ihn, and K. Ensslin, *Nano Lett.* **8**, 2547 (2008).
- ¹⁷K. D. Petersson, C. G. Smith, D. Anderson, P. Atkinson, G. A. C. Jones, and D. A. Ritchie, *Nano Lett.* **10**, 2789 (2010).
- ¹⁸J. R. Petta, A. C. Johnson, J. M. Taylor, E. A. Laird, A. Yacoby, M. D. Lukin, C. M. Marcus, M. P. Hanson, and A. C. Gossard, *Science* **309**, 2180 (2005).
- ¹⁹P. S. Eldridge, J. Hübner, S. Oertel, R. T. Harley, M. Henini, and M. Oestreich, *Phys. Rev. B* **83**, 041301 (2011).
- ²⁰K. Ono, D. G. Austing, Y. Tokura, and S. Tarucha, *Science* **297**, 1313 (2002).
- ²¹A. Pfund, I. Shorubalko, K. Ensslin, and R. Leturcq, *Phys. Rev. Lett.* **99**, 036801 (2007).
- ²²S. Nadj-Perge, S. M. Frolov, J. W. W. van Tilburg, J. Danon, Yu. V. Nazarov, R. Algra, E. P. A. M. Bakkers, and L. P. Kouwenhoven, *Phys. Rev. B* **81**, 201305 (2010).
- ²³D. Wallin, A. Fuhrer, L. E. Fröberg, L. Samuelson, H. Q. Xu, S. Hofling, and A. Forchel, *Appl. Phys. Lett.* **90**, 172112 (2007).
- ²⁴I. Shorubalko, R. Leturcq, A. Pfund, D. Tyndall, R. Krischek, S. Schön, and K. Ensslin, *Nano Lett.* **8**, 382 (2008).
- ²⁵T. Choi, I. Shorubalko, S. Gustavsson, S. Schön, and K. Ensslin, *New J. Phys.* **11**, 013005 (2009).
- ²⁶J. Sun, M. Larsson, I. Maximov, H. Hardtdegen, and H. Q. Xu, *Appl. Phys. Lett.* **94**, 042114 (2009).
- ²⁷M. Larsson, H. A. Nilsson, H. Hardtdegen, and H. Q. Xu, *Appl. Phys. Lett.* **95**, 192112 (2009).
- ²⁸J. Sun, M. Larsson, I. Maximov, and H. Q. Xu, *Appl. Phys. Lett.* **96**, 162107 (2010).
- ²⁹M. Larsson, D. Wallin, and H. Q. Xu, *J. Appl. Phys.* **103**, 086101 (2008).
- ³⁰T. Koga, J. Nitta, T. Akazaki, and H. Takayanagi, *Phys. Rev. Lett.* **89**, 046801 (2002).
- ³¹M. Field, C. G. Smith, M. Pepper, D. A. Ritchie, J. E. F. Frost, G. A. C. Jones, and D. G. Hasko, *Phys. Rev. Lett.* **70**, 1311 (1993).
- ³²A. C. Johnson, J. R. Petta, C. M. Marcus, M. P. Hanson, and A. C. Gossard, *Phys. Rev. B* **72**, 165308 (2005).
- ³³J. Danon and Yu. V. Nazarov, *Phys. Rev. B* **80**, 041301 (2009).